

26 **Nomenclature**

27 *Roman symbols*

28	A_c	Area of the chamber in plan view [m^2]
29	B^*	Dimensionless damping coefficient [–]
30	C_g	Wave group velocity [m s^{-1}]
31	C_{WR}	Capture-with ratio [–]
32	D	Diameter of the orifice that simulates the turbine [m]
33	E_p	Total pneumatic energy per unit width of converter [MWh m^{-1}]
34	E_w	Total wave energy per metre of wave front [MWh m^{-1}]
35	H_{m0}	Significant wave height [m]
36	P_p	Pneumatic power captured by the device [W]
37	P_w	Wave power per metre of wave front [W m^{-1}]
38	Q	Flow rate [m^3s^{-1}]
39	S	Spectral wave energy density [$\text{m}^2\text{Hz}^{-1}\text{rad}^{-1}$]
40	T_e	Wave energy period [s]
41	V_m	Air volume of the OWC chamber at model scale [m^3]
42	V_p	Air volume of the OWC chamber at prototype [m^3]
43	g	Gravitational acceleration [m s^{-2}]
44	h	Water depth [m]
45	k	Wave number [m^{-1}]
46	n_p	polytropic exponent of the turbine [–]
47	t_{max}	Total time of the tests [s]
48	w	Width of the OWC converter [m]

49 *Greek symbols*

50	Δp	Pressure drop [Pa]
51	δ	Tank-to-sea water density ratio [–]
52	θ_{mean}	Mean wave direction [$^\circ$]
53	λ	Linear scale factor [–]
54	ρ_a	Air density [kg m^{-3}]
55	ρ_w	Water density [kg m^{-3}]
56	ω	Wave angular frequency [rad s^{-1}]

57 *Acronyms*

58	EMEC	European Marine Energy Centre
59	BBDB	Backward Bent Duct Buoy
60	JONSWAP	Joint North Sea Wave Observation Project
61	OWC	Oscillating water column
62	RANS	Reynolds-averaged Navier–Stokes equations
63	VOF	Volume of fluid
64	WEC	Wave energy converter
65	iWEDGE	Intra-annual wave energy diagram generator

66 **1. Introduction**

67 Wave energy is one of the most promising energy sources under development, thanks to four
68 fundamental characteristics. First, the worldwide wave energy resource is vast and, importantly,
69 widely available [1,2]. Second, it can be exploited without a high impact [3]. Third, it is easily
70 predictable [4,5]. Last, but not least, its exploitation allows synergies with other marine renewables to
71 be realised [6,7]. On the downside, the wave energy resource presents significant variability on
72 different timescales, from decadal to seasonal to individual waves, which poses challenges for the
73 design and exploitation of efficient and robust wave energy converters (WECs).

74 Over the last few years, numerous works have been carried out to analyse the variability in the
75 wave energy resource, considering both inter-annual [8] and intra-annual timescales [9,10]. In
76 particular, it has been shown that the locations with the largest amount of wave energy present a great
77 intra-annual variability in the available resource [11]. This variability goes beyond a mere seasonality,
78 and monthly variations have been shown to significantly affect the performance of WECs [12,13]. It
79 follows that an intra-annual characterisation of the wave energy resource is the first step towards a
80 comprehensive evaluation of the performance of a given WEC at a site of interest. Although the
81 variability in the captured energy is typically smaller than the variability of the wave energy resource
82 itself, it remains very significant; indeed, monthly differences in the range of 156%-384% have been
83 found depending on the WEC technology [12].

84 Among the wide variety of WECs developed over the last decades, including oscillating water
85 column (OWC) devices [14], oscillating body systems [15] and overtopping converters [16], OWC
86 devices are one of the most successful. They consist of a partially submerged empty chamber open to
87 the sea below the free surface, and an air turbine. Wave action excites the water column inside the
88 chamber, which oscillates vertically, forcing the air above to alternately flow into and out of the
89 chamber, and in the process driving the turbine. Unless a rectifying system with non-return valves is
90 provided, a special turbine design, capable of operating under bidirectional flow, is required. Wells
91 (reaction) and impulse (action) turbines are typically used [17]. The simplicity of the system—only a
92 chamber and an air turbine—and its suitability for being integrated into coastal structures [18,19],
93 with the consequent benefit regarding the reduction of construction costs, are some of the main
94 advantages of OWC converters.

95 When evaluating the energy production of an OWC device at a given coastal site, which implies
96 the analysis of the performance of the converter under a wide range of sea states (irregular waves), the

97 most common solution is to make use of theoretical hydrodynamic models, both frequency-domain
98 and time-domain models. Among them, frequency-domain models are probably the most employed.
99 Although there are many examples in the recent literature, only a few are focused on evaluating the
100 energy production in a real case study. A frequency-domain stochastic model was developed in [20] to
101 calculate the annual power performance of the OWC plant on Pico Island (Portugal), equipped with a
102 Wells turbine. On this basis, a method for optimising the turbine size of the Pico OWC was proposed
103 in [21]; two alternative criteria were followed: maximum energy production and maximum
104 economical profit. The stochastic method was also used for optimising the annual power extracted by
105 a floating-type OWC converter operating in the western coast of Portugal [22]. More recently, a
106 frequency-domain hydro-thermodynamic model was proposed by [23] in order to evaluate the annual
107 energy production of a Backward Bent Duct Buoy (BBDB) floating OWC device for the wave
108 conditions off the west coast of Ireland. However, although frequency-domain models are
109 computationally undemanding, they present the disadvantage of being limited to linear problems, i.e.,
110 those involving small amplitude waves and linear turbines (e.g., Wells).

111 On the other hand, time-domain models allow the consideration of non-linear effects as well as
112 the analysis of non-linear turbines (e.g., impulse turbines). A time-domain model for a BBDB device
113 off the west coast of Vancouver Island (Canada) was presented in [24]; the model includes some non-
114 linear effects namely: mooring forces, viscous drag and air compressibility, which were found of great
115 importance for adequately modelling the converter. The performance of the OWC plant at the
116 breakwater of Mutriku (Spain) was also investigated through time-domain models. First, in [25] the
117 annual average performances of two air turbines, a Wells turbine and a biradial turbine [26], were
118 compared. Second, in [27] the influence on the power production performance of the plant of three
119 speed control strategies for the biradial turbine was analysed. Finally, a time-domain model was
120 developed in [28] for evaluating the annual power performance of the Tupperwave floating OWC
121 device and compared to that of a conventional floating OWC, both located at the European Marine
122 Energy Centre (EMEC) wave energy test site, off the coast of Scotland.

123 When a most accurate analysis is needed, two alternatives emerge: (i) computational fluid
124 dynamic (CFD) models based on the Reynolds-averaged Navier–Stokes (RANS) equations, and (ii)
125 physical models. RANS models, with the help of a turbulence closure model, determine the velocity
126 fields on the entire domain, being capable of solving the non-linear wave-converter interactions,
127 including complex phenomena such as wave breaking. Moreover, by using the volume of fluid (VOF)

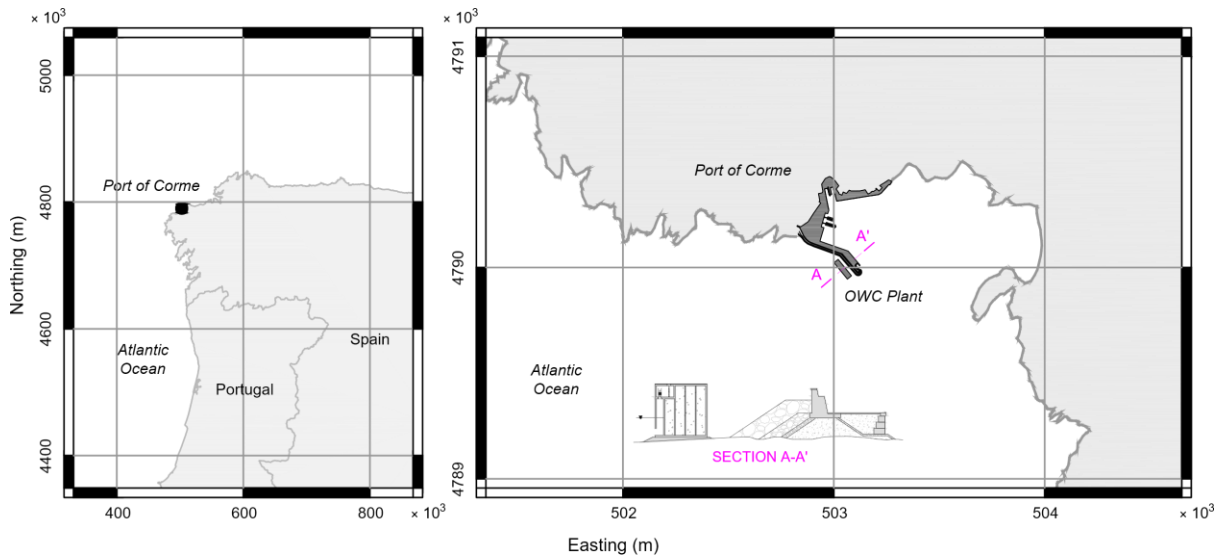
128 technique [29], these models manage to accurately capture the air-water interface. A RANS-VOF
129 numerical model was applied to study the annual energy capture of an OWC plant at the breakwater
130 of A Guarda (Spain) in [30]. Similarly, the annual performance of a breakwater-integrated OWC
131 converter on the southern Brazilian coast was evaluated through a RANS-VOF model [31]. Regarding
132 physical model tests, they are still one of the best options in order to obtain trustworthy results,
133 avoiding numerical approximations and uncertainties and high computational times. Physical
134 modelling was used for evaluating the annual energy capture of an OWC device at three different
135 locations in the north west coast of Spain [32].

136 Despite the great number of models presented above for evaluating the energy production of an
137 OWC device at a given coastal site, all of them analyse the energy production of the device in annual
138 average figures. Taking into account the fact that the performance of an OWC depends on both the
139 wave conditions and the turbine-induced damping [33], and considering that the variability in the
140 wave conditions is typically large in the areas of interest for wave energy exploitation, the intra-
141 annual variability in the performance of an OWC and its relationship with the turbine-induced
142 damping must be investigated—and therein lies the motivation and novelty of the present work.

143 The methodology followed in the present piece of research combines numerical and physical
144 modelling. First, the intra-annual wave energy resource characterisation matrices at a location of
145 interest—for illustration, a case study in NW Spain was considered—were computed through high-
146 resolution spectral numerical modelling based on the energy bin concept. Second, the efficiency
147 matrices of the OWC wave energy converter were determined by means of physical modelling—
148 therefore, considering non-linear effects—taking into account specifically the influence of air
149 compressibility and considering three (non-linear) impulse turbines of different characteristics,
150 emulated through three values of the turbine-induced damping, an essential parameter to be
151 considered when studying OWC devices [34,35]. Lastly, the intra-annual energy capture matrices (one
152 per each turbine-induced damping) were computed by combining the intra-annual resource matrices
153 with the efficiency matrices of the device. The paper is organized as follows. In Section 2, the location
154 and main characteristics of the study site are presented. The methodology is described in Section 3,
155 and the results of its application to the case study are described and discussed in Section 4. Finally, the
156 main conclusions are summarised in Section 5.

157 **2. Study site**

158 The installation of an OWC in Corme, a medium-size port in Galicia (NW Spain), was considered for
159 the study (Figure 1). Corme is in the coastal stretch known as the Death Coast, extending from Cape
160 Finisterre to the Sisargas Isles. The entrance of the port is located at a depth of approx. 12 m at mid
161 tide. This area stands out for its vast wave energy resource [36], which is subject to a very significant
162 intra-annual variability [9]. For these reasons Corme is well suited as a case study for this research.



163
164 Figure 1. Location of the study site, the Port of Corme, with a sketch of the proposed OWC device
165 (coordinate reference system ETRS89 - UTM zone 29N).

166 **3. Materials and methods**

167 3.1. Numerical model

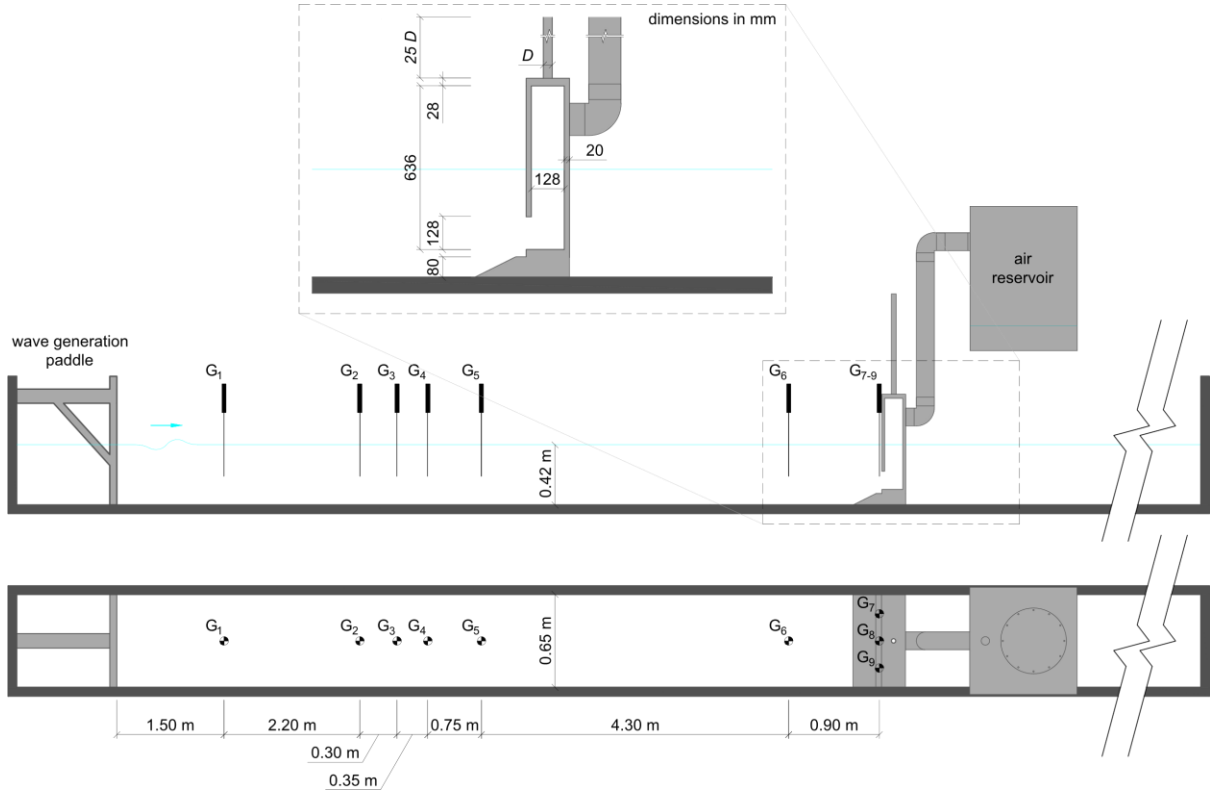
168 As established in Section 1, an appropriate analysis of the intra-annual variability in the performance
169 of an OWC at location of interest should be conducted based on a thorough knowledge of the existing
170 wave conditions at this specific site. The information required for this analysis should consist of
171 characterization matrices with the same level of resolution as that of the efficiency matrix of the OWC
172 and covering time periods short enough in order to appropriately characterise the intra-annual
173 variation of the wave resource, which in turn may well lead to significant intra-annual variations in
174 the performance of the OWC considered.

175 With this in view, the methodology iWEDGE (intrannual Wave Energy Diagram Generator)
176 [9,12] is used in order to obtain the required information at the selected location. The methodology is
177 based on the energy bin concept, or energy intervals describing the available energy and occurrence of
178 combinations of the relevant wave spectral parameters. The implementation of this procedure is

179 divided in three main steps. First, the deepwater wave energy resource in the area of interest is
180 characterized by analysing deepwater in situ data recorded by the Silleiro's deepwater buoy, being the
181 result a 3D characterization matrix providing the distribution of the total energy available along with
182 its intra-annual occurrence amongst trivariate energy bins, i.e., energy bins whose intervals are
183 defined by combinations of significant wave height (H_{m0}), energy period (T_e), and mean wave
184 direction (θ_{mean}). In the second step, the most energetic bins providing 95% of the total wave energy
185 resource are propagated towards the coastal location of interest by means of high-resolution spectral
186 numerical modelling. Finally, the resulting wave conditions of H_{m0} and T_e for all the energy bins
187 propagated are obtained at the grid node closest to the selected location. This information together
188 with the intra-annual occurrence of each selected bin is used to reconstruct 2D characterization
189 matrices composed of bivariate energy bins (or energy intervals of H_{m0} and T_e), i.e., the required
190 information for conducting accurate intra-annual performance analysis [12,37].

191 3.2. Physical model

192 The experimental campaign was performed in the wave flume of the University of Santiago de
193 Compostela. The tests were carried out at a 1:25 scale. The experimental set-up and the geometry of
194 the model are depicted in Figure 2. Nine wave gauges located along the flume and two ultrasonic
195 level sensors located in the interior of the chamber were set to monitor the free surface elevations and
196 the oscillations of the water column. Moreover, a differential pressure sensor was allocated to monitor
197 the relative pressure inside the chamber.



198
199

Figure 2. Side and plan view of the experimental set-up.

200 The OWC model follows, in its submerged part, the Froude similitude criterion—*sine qua non*
 201 condition when free-surface flows are involved [38]—and full geometrical similarity. However, for
 202 correctly modelling air compressibility effects, which are essential to avoid significant errors in the
 203 evaluation of the performance of an OWC device [39,40], the air volume in the chamber (V) must be
 204 scaled according to [41]:

205
$$\frac{V_p}{V_m} = \lambda^2 n_p \delta, \quad (1)$$

206 where the subscripts p and m indicate prototype and model, respectively; λ is the linear scale factor; n_p
 207 is the polytropic exponent of the turbine; and δ is the water density ratio. Thus, a distorted aerial part
 208 was set to accomplish a total air volume in the chamber of, according to Eq.(1), $V_m = 538.4 \text{ dm}^3$. As
 209 shows Figure 2, the extra air volume was achieved by connecting an air reservoir to the OWC model
 210 chamber [41].

211 Amongst the two most common OWC turbines (Wells and impulse), the self-rectifying impulse
 212 turbines were chosen in this work due to the fact that its average efficiency is kept practically
 213 unchanged within a wide range of sea states and, in addition, they present a lower level of noise in
 214 comparison with Wells turbines [17], which is an important feature for port-located OWC devices.

215 Impulse turbines present a quadratic pressure-vs-flowrate relation [42]. Therefore, the turbine-induced
 216 damping was modelled through orifices of different diameter [43,44]. Unlike with Wells turbines,
 217 with self-rectifying impulse turbines the turbine-induced damping barely depends on the rotational
 218 speed of the turbine [14], and therefore a turbine of a given diameter can be simulated through a
 219 single orifice for the complete range of operating conditions. The orifices were characterised by
 220 means of the damping coefficient, defined as

$$221 \quad B^* = \frac{\Delta p^{1/2}}{Q} \frac{A_c}{\rho_a^{1/2}}, \quad (2)$$

222 where Δp is the pressure drop between the interior of the chamber and the atmosphere; Q is the flow
 223 rate through the orifice; A_c is the area of the chamber in plan view; and ρ_a is the density of air. The
 224 ratio $\Delta p^{1/2} Q^{-1}$ was obtained following López *et al.* [32]. A summary of the different parameters that
 225 characterise the orifices is presented in Table 1.

226 Table 1. Diameter (D), opening ratio (ratio between the area of the orifice and the plan area of
 227 the chamber), pressure-vs-flowrate relation ($\Delta p^{1/2} Q^{-1}$) and damping coefficient (B^*) for the
 228 different orifice diameters tested.

D (mm)	Opening ratio (%)	$\Delta p^{1/2} Q^{-1}$ (kgm ⁻⁷)	B^* (-)
39	1.5	1.48×10^6	84.85
31	1.0	3.59×10^6	132.18
28	0.8	5.30×10^6	160.49

229 The testing programme comprised forty-nine irregular wave conditions, resulting from the
 230 combination of five significant wave heights, ($H_{m0} = 0.79, 1.65, 2.60, 3.57$ and 4.55 m) and eleven
 231 energy periods ($T_e = 4.5, 5.5, 6.5, 7.5, 8.5, 9.5, 10.5, 11.5, 12.5, 13.5$ and 14.5 s). These wave
 232 conditions, generated following a JONSWAP-type spectra [45], are representative of an equal number
 233 of energy bins (Figure 3).

234 The efficiency of the OWC device under each wave condition was evaluated based on the
 235 capture-width ratio, defined as:

$$236 \quad C_{WR} = \frac{P_p}{P_w w}, \quad (3)$$

237 where w is the width of the device (dimension orthogonal to the incident wave direction); P_p is the
 238 pneumatic power captured by the device, calculated following

$$239 \quad P_p = \frac{1}{t_{max}} \int_0^{t_{max}} \Delta p(t) Q(t) dt, \quad (4)$$

240 where t_{max} is the total time of the test.

241 Finally, P_w is the incident wave power per metre of wave front, defined as:

242
$$P_w = \rho_w g \int_0^\infty S(\omega) C_g(\omega) d\omega , \quad (5)$$

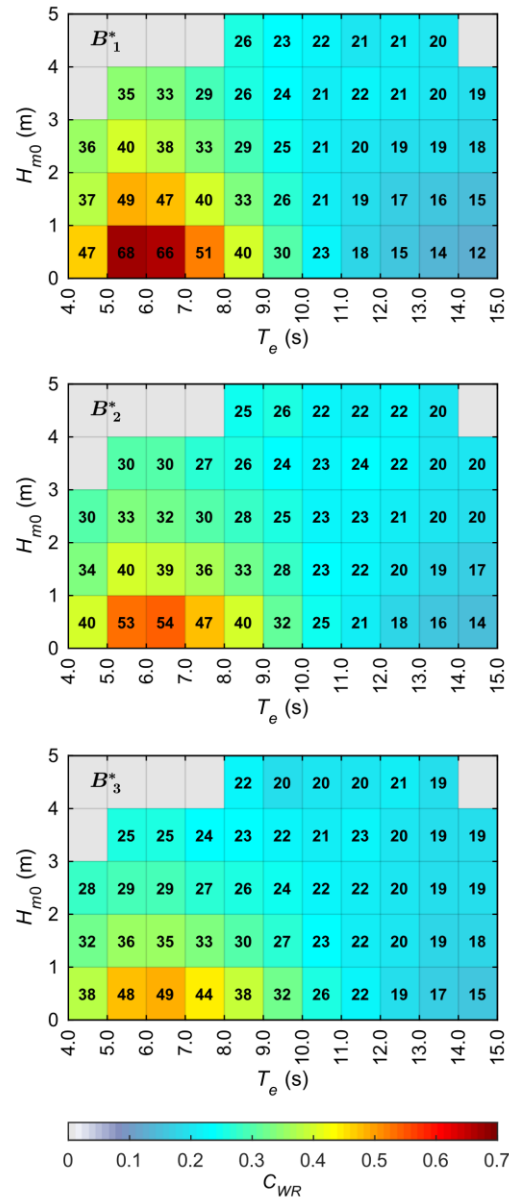
243 where ρ_w is the water density; g is the gravitational acceleration; $S(\omega)$ is the spectral density of the
 244 incident wave; and C_g is the group velocity defined as

245
$$C_g(\omega) = \frac{1}{2} \frac{\omega_i}{k_i} \left(1 + \frac{2k_i h}{\sinh 2k_i h} \right), \quad (6)$$

246 where ω_i and k_i are the angular frequency and the wave number of each i th frequency band; and h is
 247 the water depth. The wave number is related to the angular frequency through the dispersion relation:

248
$$\omega_i^2 = g k_i \tanh k_i h . \quad (7)$$

249 The efficiency of all the sea states included within the intervals of an energy bin is assumed to be
 250 the same, being all of them characterised by the most representative wave condition previously
 251 selected. Therefore, the capture-width ratios of the forty-nine wave conditions define, for each value
 252 of the damping coefficient, the efficiency matrices of the OWC (Figure 3). A comprehensive
 253 description of the experimental tests can be found in [32].



254

255

256

Figure 3. OWC efficiency matrices expressed in term of the capture-width ratio (C_{WR}) for the three values of the turbine-induced damping tested ($B^*_1 = 84.85$; $B^*_2 = 132.18$; $B^*_3 = 160.49$).

257 **4. Results and discussion**

258 4.1. Intra-annual wave resource

259 The intra-annual wave resource characterisation matrices corresponding to the location of interest are
 260 presented for the months of January, April, July and October (Figure 4) with a view to covering the
 261 four seasons. A great intra-annual variability in the wave energy resource can be clearly observed.

262 Among the represented months, January is the one that presents the largest amount of wave energy, as
 263 shown by the more reddish colours (more wave energy available) of its energy bins. In this month, the
 264 bulk of energy is provided by sea states with significant wave heights between 1 and 3 m, and energy

265 periods between 9 and 10 s. In addition, the wave energy resource is distributed over a wide range of
266 wave heights up to 4 m. In October, although the wave energy is distributed again over sea states with
267 wave height up to 4 m, the wave energy provided is lower than in January (yellowish colours of the
268 energy bins). The largest amount of energy is provided by sea states with significant wave heights
269 between 1 and 2 m, and energy periods between 8 and 9 s. The wave energy is even lower in April. In
270 this month, the bulk of energy is provided by sea states of similar characteristics to those in October
271 ($1 \text{ m} < H_{m0} < 2 \text{ m}$ and $8 \text{ s} < T_e < 9 \text{ s}$). The wave energy resource, however, is distributed over a
272 comparatively narrower range of wave heights ($0 \text{ m} < H_{m0} < 3 \text{ m}$). Finally, July is the month with the
273 lowest wave energy of the four analysed. The resource is distributed in the narrowest range of wave
274 heights of all the months ($0 \text{ m} < H_{m0} < 2 \text{ m}$), and the bulk of energy is provided by energy bins in the
275 range $0 \text{ m} < H_{m0} < 1 \text{ m}$ and $6 \text{ s} < T_e < 7 \text{ s}$.

276 In sum, the wave energy resource distribution varies along the year going from a typical winter
277 situation (e.g., January) in which the largest amount of energy is provided by sea states with energy
278 periods between 9 and 10 s and significant wave heights between 1 and 2 m, to a typical summer
279 situation (e.g., July) in which the largest amount of energy is provided by sea states with energy
280 periods between 6 and 7 s and significant wave heights between 0 and 1 m, with an intermediate
281 situation in the remaining months (e.g., April and October). That is, the bulk of energy moves towards
282 lower energy periods and wave heights during summer months.

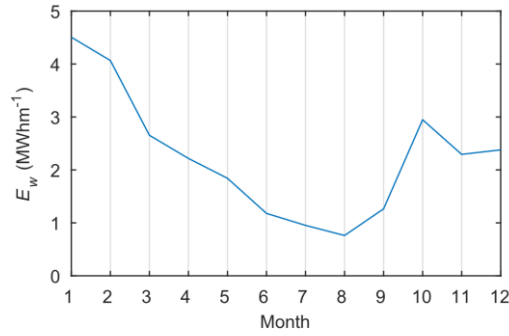
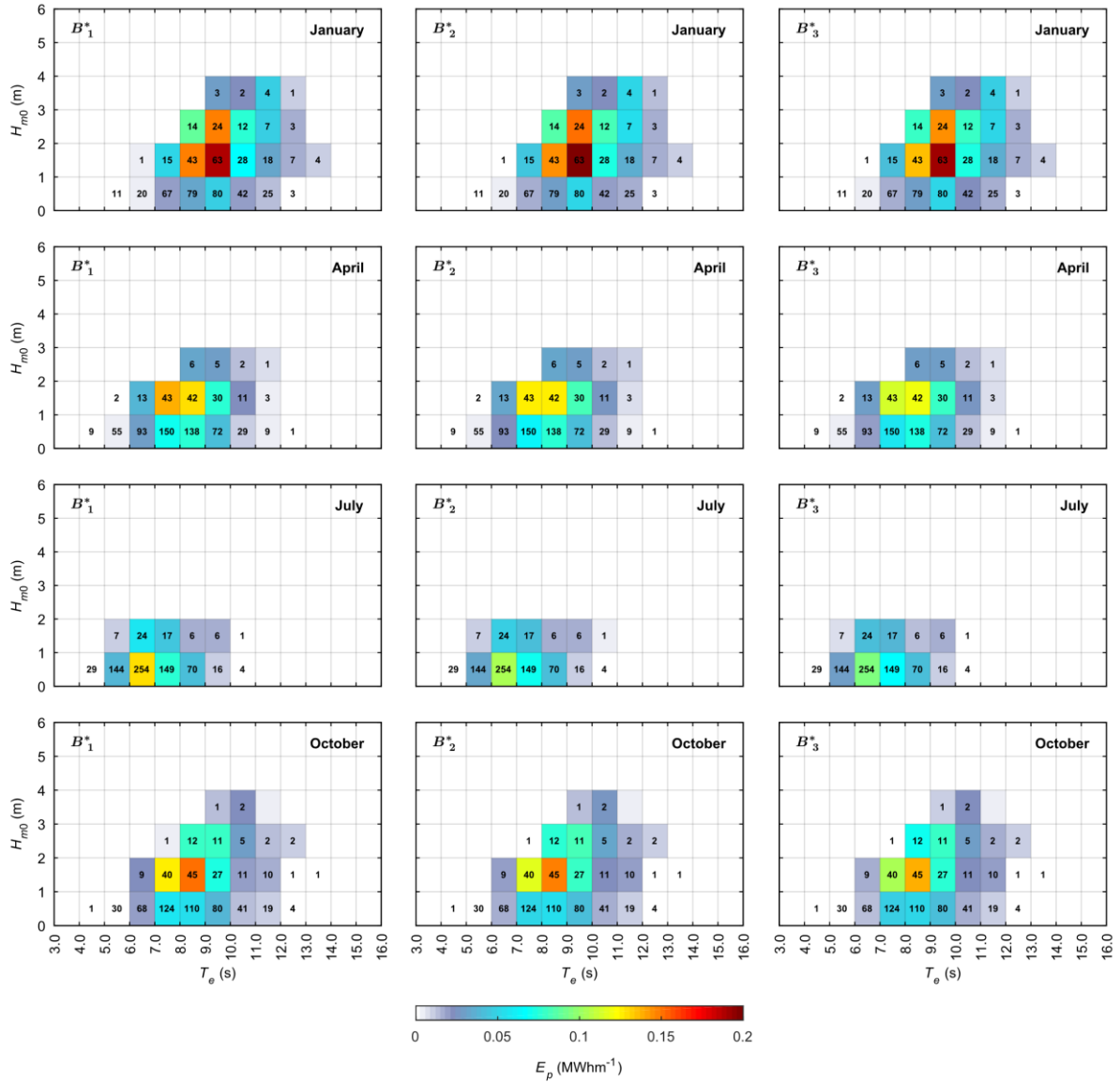


Figure 5. Intra-annual wave energy resource in an average year.

299
300

301 4.2. Intra-annual variability in the OWC performance

302 The combination of the OWC efficiency matrices (Figure 3) with the intra-annual resource matrices
 303 (Figure 4) is presented in Figure 6 for the months of January, April, July and October. The great
 304 influence of the wave energy resource on the captured energy is apparent; in fact, the energy bins that
 305 provide the bulk of captured energy match those providing the largest amount of available energy for
 306 the three values of the damping. For example, in January the energy bin which supplies the largest
 307 amount of captured energy is delimited, for the three values of the turbine-induced damping, by
 308 energy periods between 9 and 10 s and significant wave heights between 1 and 2 m, corresponding to
 309 the energy bin contributing the most to the available energy resource in that month (Figure 4). An
 310 analogous situation takes place in July and October. Interestingly, in April the turbine-induced
 311 damping presents a comparatively higher influence, i.e., the energy bin which supplies the largest
 312 amount of captured energy changes depending on the value of the damping coefficient. Thus, for the
 313 highest damping (B^*_3) the energy bin that supplies the largest amount of captured energy is bounded
 314 by $8 \text{ s} < T_e < 9 \text{ s}$ and $1 \text{ m} < H_{m0} < 2 \text{ m}$; for the lowest damping (B^*_1) it is bounded by $7 \text{ s} < T_e < 8 \text{ s}$
 315 and $1 \text{ m} < H_{m0} < 2 \text{ m}$; finally, for the intermediate damping (B^*_2), the two aforementioned energy bins
 316 provide virtually the same captured energy. In any case, even in those months in which the energy bin
 317 that supplies the largest amount of captured energy does not change with the turbine-induced
 318 damping, the influence of this factor on the captured energy is unequivocally high. For example, in
 319 July, paying attention to the energy bin that supplies the largest amount of captured energy, the highest
 320 damping coefficient provides 26% less captured energy ($E_{p, jul} = 0.10 \text{ MWhm}^{-1}$) than the lowest one
 321 ($E_{p, jul} = 0.13 \text{ MWhm}^{-1}$).



322
323
324
325
326

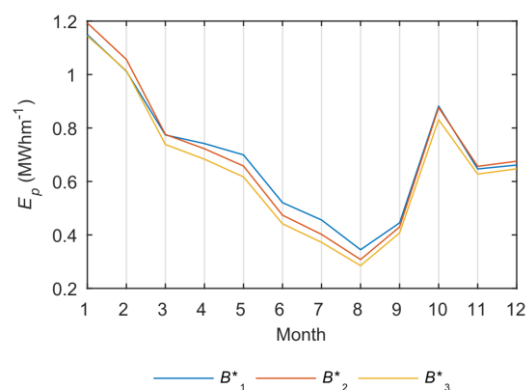
Figure 6. Intra-annual energy capture matrices of the OWC for the three values of the damping coefficient ($B^*_1 = 84.85$; $B^*_2 = 132.18$; $B^*_3 = 160.49$) and four months. The colour scale indicates the total pneumatic energy per unit width of converter absorbed by the device in each energy bin (E_p) and the numbers provide the occurrence, in hours, of the sea states within that bin.

327
328
329
330
331
332
333

Instead of considering individual energy bins, it may be interesting to analyse the intra-annual variability of the OWC performance for the entire wave climate (Figure 7). Given that, first, there is a great intra-annual variability throughout the year (Figure 5), and second, the captured energy is highly influenced by the available energy [32], the great variability in the intra-annual captured energy (Figure 7) is to be expected. The total annual captured energy changes as a function of the value of the damping coefficient from $E_{w, annual} = 8.3 MWhm^{-1}$ for B^*_1 , to $E_{w, annual} = 8.2 MWhm^{-1}$ for B^*_2 , and $E_{w, annual} = 7.8 MWhm^{-1}$ for B^*_3 . The increase in the captured energy between the least and the most

334 energetic months is of 230%, 290% and 300% for B^*_1 , B^*_2 , and B^*_3 , respectively, i.e., the lower the
 335 value of the damping coefficient, the lower the intra-annual variability in the captured energy, which
 336 emphasises again the influence of the turbine-induced damping on the intra-annual variability in the
 337 captured energy. Comparing these values with the increase on the available energy between the least
 338 and the most energetic months mentioned above, it can be seen that the variability in the intra-annual
 339 captured energy is lower than in the intra-annual available energy, for the three values of the turbine-
 340 induced damping.

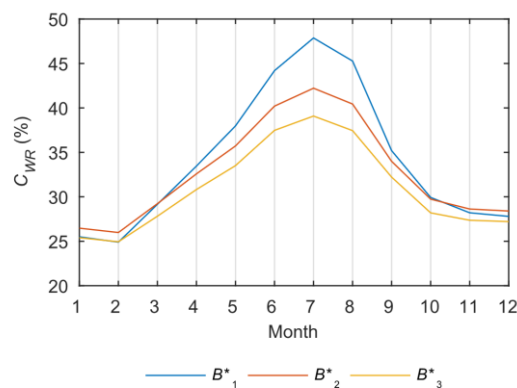
341 The lower variability shown by the intra-annual captured energy in comparison with that of the
 342 intra-annual available energy is related to the configuration of the efficiency matrices, in which sea
 343 states with high wave heights and medium to large periods (high-power sea states) present lower
 344 values of the capture-width ratio than sea states with low wave heights and periods (low-power sea
 345 states). High-power sea states are common in winter months when the available wave energy is higher
 346 and low-power sea states are common in summer months when the available energy is lower (Figure 4
 347 and Figure 5), a fact which tends to reduce the variability in the intra-annual captured energy. Here, an
 348 interesting point arises: in order to reduce the intra-annual variability in the captured energy, it is
 349 necessary to maximise the performance of the device in the months with the lowest resource. Taking
 350 into account that, as shown above in Figure 4, the wave energy resource distribution varies throughout
 351 the year in such a way that the bulk of energy moves towards lower energy periods and wave heights
 352 during summer months, this optimisation process should be conducted when designing the converter
 353 for an specific coastal location.



354
 355 Figure 7. Intra-annual pneumatic energy captured by the OWC in an average year for the three values
 356 of the damping coefficient ($B^*_1 = 84.85$; $B^*_2 = 132.18$; $B^*_3 = 160.49$).

357 The intra-annual capture-width ratio is presented for the three values of the damping coefficient
 358 in Figure 8. It can be clearly seen that, as pointed above, the intra-annual capture-width ratio follows

359 an inverse trend of that of the intra-annual available energy (Figure 5), which reduces the variability
 360 in the intra-annual captured energy when comparing with the intra-annual available energy. Therefore,
 361 the present OWC converter constitutes a good design for reducing the intra-annual variability in the
 362 captured energy. This result applies to the three values of the damping, although with different
 363 intensity: the lower the value of the damping coefficient, the higher the intra-annual variability in the
 364 capture-width ratio. Furthermore, it can be seen that the value of the damping coefficient that
 365 performs best in each month varies throughout the year (Figure 8). In January, February, November
 366 and December the intermediate damping (B^*_2) achieves the higher values of the capture-width ratio.
 367 From April to September, the lowest damping (B^*_1) performs best. In March and October both values
 368 of the damping coefficient, B^*_1 and B^*_2 , provide virtually equal values of the capture-width ratio. The
 369 highest damping (B^*_3), however, does not provide the best performance in any month, thereby its use
 370 is inadvisable at this particular site.

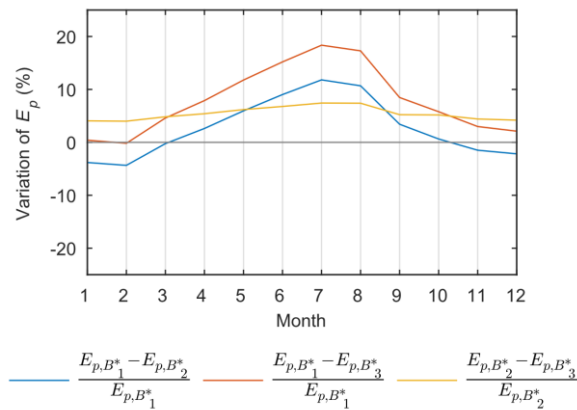


371
 372 Figure 8. Intra-annual capture-width ratio (C_{WR}) of the OWC in an average year for the three values of
 373 the damping coefficient ($B^*_1 = 84.85$; $B^*_2 = 132.18$; $B^*_3 = 160.49$).

374 As regards the intra-annual captured energy, the turbine-induced damping also plays an
 375 important role. In order to appropriately analyse its influence, in Figure 9 the intra-annual variation of
 376 the relative difference in the energy captured by the OWC is presented for two values of the damping
 377 coefficient. When the OWC is operating with the lowest damping, the captured energy increases
 378 throughout the year (with the exception of February) if comparing with the captured energy under the
 379 highest damping; the greatest differences are achieved in July with an increase of the captured energy
 380 of 18.4%. When comparing the performance of the lowest damping with respect to the intermediate
 381 one, there is an increase of the captured energy starting in April with 2.6%, progressively rising up to
 382 a maximum of 11.8% in July and, from that point on, progressively reducing again down to 0.6% in

383 October; in the months of January, February, March, November and December the captured energy
 384 decreases in percentages always below 4.3%, with this minimum value being attained in February.

385 These results add another criterion for selecting the optimum damping for a given study site. In
 386 the present case, in which the total annual captured energy is very close for the lowest and
 387 intermediate values of the damping coefficient ($E_{w, annual} = 8.3 \text{ MWhm}^{-1}$ and $E_{w, annual} = 8.2 \text{ MWhm}^{-1}$,
 388 respectively), the lower variability in the intra-annual captured energy achieved by the lowest
 389 damping (Figure 7) reinforces the selection of the lowest turbine-induced damping as the best
 390 performing one. What is more, even in those cases in which the total annual captured energy is
 391 slightly greater for a given value of the damping coefficient, it could be interesting to select another
 392 damping coefficient if it ensures a greater amount of captured energy in summer months, or what is
 393 the same, a lower variability in the intra-annual captured energy. This could be the case of the energy
 394 supply on an off-grid system, e.g., an island, in which the provision of energy all over the year is of
 395 paramount importance. Is this situation, the converter should be designed in order to minimise the
 396 intra-annual variability in the captured energy. The requirement is to supply sufficient energy
 397 throughout the year. Thus, the analysis cannot be focused on achieving great annual numbers of
 398 captured energy but harnessing enough energy in the months in which the resource is scarce. At this
 399 point, knowing the intra-annual electricity demand could shed light on determining the most
 400 disadvantageous month.



401
 402 Figure 9. Intra-annual variation of the relative difference between the energy captured by the OWC for
 403 two different values of the damping coefficient.

404 Finally, based on the results achieved, the question arises as to whether the turbine-induced
 405 damping could be adapted for matching the optimum damping on a monthly basis, thereby
 406 maximising the captured energy. This is not possible with self-rectifying impulse turbines given that

407 the damping is mainly determined by the turbine diameter (an invariable parameter) and virtually
408 independent of the rotational speed [14]. This impossibility, i.e., the fact that the turbine-induced
409 damping is constant during the entire life of the turbine, makes it all the more important to apply an
410 intra-annual analysis to select the most appropriate value. Moreover, from the point of view of the
411 turbine efficiency, adjusting the rotational speed without modifying the turbine-induced damping is an
412 important benefit, because the turbine rotational speed can be optimised without affecting the
413 hydrodynamic performance of the chamber. A different situation occurs in the case of an OWC
414 equipped with a Wells turbine, whose rotational speed affects the damping exerted on the system [14],
415 enabling the adjustment of the turbine-induced damping depending on the month. However, a careful
416 and complex analysis is necessary given that, when the damping of the turbine changes, the efficiency
417 of the hydrodynamic process of wave energy absorption also changes. This is a topic that deserves
418 further study; however, it is out of the scope of this work, since a different methodology capable of
419 emulating a linear turbine and different values of the damping coefficient must be applied depending
420 on the rotational speed of the turbine.

421 **5. Conclusions**

422 In this work a methodology based on a combination of numerical and physical modelling—thus,
423 considering non-linear effects, and in particular air compressibility—was applied to comprehensively
424 analyse a usually disregarded factor when evaluating the energy production of an OWC wave energy
425 converter at a given coastal site: the intra-annual variability in the performance of the device. To this
426 end, the intra-annual variability in the performance of an OWC wave energy converter was
427 comprehensively analysed through a case study in Galicia (NW Spain). First, numerical modelling
428 was used to characterise, by means of a high-resolution procedure, the intra-annual wave energy
429 resource, which yielded site-specific intra-annual characterisation matrices. Second, physical
430 modelling was used to obtain the three efficiency matrices of the OWC converter (one per each value
431 of turbine-induced damping considered). Finally, the intra-annual energy capture matrices were
432 computed by combining the resource and efficiency matrices.

433 It was found that the wave energy resource at the study site presents significant intra-annual
434 variability. Between the month with the lowest (July) and the greatest (January) available energy the
435 difference is over 400%. Importantly, not only the amount of available energy varies but also its
436 distribution across sea states: in winter the bulk of energy is provided by sea states with energy

437 periods in the range $9 \text{ s} < T_e < 10 \text{ s}$ and significant wave heights in the range $1 \text{ m} < H_{m0} < 3 \text{ m}$; these
438 ranges evolve towards lower energy periods and lower significant wave heights in summer
439 ($6 \text{ s} < T_e < 7 \text{ s}$, and $0 \text{ m} < H_{m0} < 1 \text{ m}$, respectively). As both parameters (energy period and significant
440 wave height) greatly influence the capture-width ratio of the OWC, it follows that a high-resolution
441 intra-annual wave energy characterisation is fundamental to correctly characterise the performance of
442 an OWC throughout the year.

443 Regarding the intra-annual variability in the energy captured, the following conclusions may be
444 drawn. First, the intra-annual captured energy follows the same trend as the intra-annual available
445 energy. However, the variability in the intra-annual captured energy is slightly weaker thanks to the
446 design of the OWC, that exhibits a better performance when the available energy is lower, that is, in
447 summer months—characterised by lower energy periods and smaller significant wave heights, for
448 which the capture-width ratios are higher. Second, the intra-annual variability in the captured energy
449 changes its intensity depending on the damping coefficient, which adds another criterion for selecting
450 the optimum damping for a given study site. In the study case, the lower the value of the damping
451 coefficient, the lower the variability in the captured energy. Finally, it was found that the turbine-
452 induced damping which maximises the energy capture of the OWC is not constant, and depends on
453 the succession of sea states in the period considered for the maximisation; in the study case,
454 considering monthly periods, the optimum value varied from one month to the next. Taking the entire
455 year as the period for the maximisation of the energy capture, the lowest value of the damping
456 coefficient ($B^*_1 = 84.85$) was found to be the best of those considered, for it provided the largest
457 annual captured energy along with the lowest intra-annual variability.

458 In sum, the turbine-induced damping ought to be regarded as one of the fundamental elements
459 when designing an OWC plant, as it significantly affects the energy capture. However, an inter-annual
460 analysis is not enough, given that the damping that maximises the performance of the OWC changes
461 on a monthly basis. Therefore, to select the most appropriate turbine-induced damping overall—that
462 is, for dimensioning the turbine—for a given site of interest both the turbine-induced damping and a
463 high-resolution characterisation of the wave energy resource, carried out at an intra-annual level, are
464 in order.

465 **Acknowledgements**

466 During this work I. López was supported by the postdoctoral grant ED481D 2019/019 of the
467 ‘Programa de Axudas á etapa posdoutoral da Xunta de Galicia (Consellería de Educación,
468 Universidade e Formación Profesional)’.

469 **References**

- 470 [1] López M, Veigas M, Iglesias G. On the wave energy resource of Peru. *Energy Conv Manag*
471 2015;90:34-40. <https://dx.doi.org/10.1016/j.enconman.2014.11.012>
- 472 [2] Weiss CVC, Guanche R, Ondiviela B, Castellanos OF, Juanes J. Marine renewable energy
473 potential: A global perspective for offshore wind and wave exploitation. *Energy Conv Manag*
474 2018;177:43-54. <https://doi.org/10.1016/j.enconman.2018.09.059>
- 475 [3] O'Dea A, Haller MC, Özkan-Haller HT. The impact of wave energy converter arrays on wave-
476 induced forcing in the surf zone. *Ocean Eng*
477 2018;161:322-36. <https://doi.org/10.1016/j.oceaneng.2018.03.077>
- 478 [4] Perez J, Menendez M, Losada IJ. GOW2: A global wave hindcast for coastal applications. *Coast*
479 *Eng* 2017;124:1-11. <https://doi.org/10.1016/j.coastaleng.2017.03.005>
- 480 [5] Lavidas G, Venugopal V. A 35 year high-resolution wave atlas for nearshore energy production
481 and economics at the Aegean Sea. *Renew Energy* 2017;103:401-17.
482 <https://doi.org/10.1016/j.renene.2016.11.055>
- 483 [6] Zheng S, Zhang Y, Iglesias G. Coast/breakwater-integrated OWC: A theoretical model. *Mar Struct*
484 2019;66:121-35. <https://doi.org/10.1016/j.marstruc.2019.04.001>
- 485 [7] Perez-Collazo C, Pemberton R, Greaves D, Iglesias G. Monopile-mounted wave energy converter
486 for a hybrid wind-wave system. *Energy Conv Manag*
487 2019;199:111971. <https://doi.org/10.1016/j.enconman.2019.111971>
- 488 [8] Ramos V, López M, Taveira-Pinto F, Rosa-Santos P. Influence of the wave climate seasonality on
489 the performance of a wave energy converter: A case study. *Energy* 2017;135:303-16.
490 <https://doi.org/10.1016/j.energy.2017.06.080>
- 491 [9] Carballo R, Sánchez M, Ramos V, Fragueta JA, Iglesias G. Intra-annual wave resource
492 characterization for energy exploitation: A new decision-aid tool. *Energy Conv Manag*
493 2015;93:1-8. <https://doi.org/10.1016/j.enconman.2014.12.068>
- 494 [10] Carballo R, Iglesias G. A methodology to determine the power performance of wave energy
495 converters at a particular coastal location. *Energy Conv Manag* 2012;61:8-18.
496 <https://dx.doi.org/10.1016/j.enconman.2012.03.008>
- 497 [11] Neill SP, Hashemi MR. Wave power variability over the northwest European shelf seas. *Appl*
498 *Energy* 2013;106:31-46. <https://dx.doi.org/10.1016/j.apenergy.2013.01.026>
- 499 [12] Carballo R, Sánchez M, Ramos V, Fragueta JA, Iglesias G. The intra-annual variability in the
500 performance of wave energy converters: A comparative study in N Galicia (Spain). *Energy*
501 2015;82:138-46. <https://doi.org/10.1016/j.energy.2015.01.020>

- 502 [13] Guillou N, Chapalain G. Annual and seasonal variabilities in the performances of wave energy
503 converters. *Energy* 2018;165:812-23. <https://doi.org/10.1016/j.energy.2018.10.001>
- 504 [14] Falcão AFO, Henriques JCC. Oscillating-water-column wave energy converters and air turbines:
505 A review. *Renew Energy* 2016;85:1391-424. <https://dx.doi.org/10.1016/j.renene.2015.07.086>
- 506 [15] Chen F, Duan D, Han Q, Yang X, Zhao F. Study on force and wave energy conversion efficiency
507 of buoys in low wave energy density seas. *Energy Conv Manag*
508 2019;182:191-200. <https://doi.org/10.1016/j.enconman.2018.12.074>
- 509 [16] Oliveira P, Taveira-Pinto F, Morais T, Rosa-Santos P. Experimental evaluation of the effect of
510 wave focusing walls on the performance of the Sea-wave Slot-cone Generator. *Energy Conv*
511 *Manag* 2016;110:165-75. <https://doi.org/10.1016/j.enconman.2015.11.071>
- 512 [17] Falcão AFO, Henriques JCC, Gato LMC. Self-rectifying air turbines for wave energy
513 conversion: A comparative analysis. *Renew Sust Energ Rev* 2018;91:1231-41.
514 <https://doi.org/10.1016/j.rser.2018.04.019>
- 515 [18] Strati FM, Malara G, Arena F. Performance optimization of a U-Oscillating-Water-Column wave
516 energy harvester. *Renew Energy* 2016;99:1019-28. <https://doi.org/10.1016/j.renene.2016.07.080>
- 517 [19] Zheng S, Antonini A, Zhang Y, Greaves D, Miles J, Iglesias G. Wave power extraction from
518 multiple oscillating water columns along a straight coast. *J Fluid Mech* 2019;878:445-80.
519 <http://dx.doi.org/10.1017/jfm.2019.656>
- 520 [20] Falcão AFO, Rodrigues RJA. Stochastic modelling of OWC wave power plant performance.
521 *Appl Ocean Res* 2002;24:59-71. [https://doi.org/10.1016/S0141-1187\(02\)00022-6](https://doi.org/10.1016/S0141-1187(02)00022-6)
- 522 [21] Falcão AFO. Stochastic modelling in wave power-equipment optimization: maximum energy
523 production versus maximum profit. *Ocean Eng* 2004;31:1407-21.
524 <http://dx.doi.org/10.1016/j.oceaneng.2004.03.004>
- 525 [22] Gomes RPF, Henriques JCC, Gato LMC, Falcão AFO. Hydrodynamic optimization of an
526 axisymmetric floating oscillating water column for wave energy conversion. *Renew Energy*
527 2012;44:328-39. <https://doi.org/10.1016/j.renene.2012.01.105>
- 528 [23] Sheng W. Power performance of BBDB OWC wave energy converters. *Renew Energy*
529 2019;132:709-22. <https://doi.org/10.1016/j.renene.2018.07.111>
- 530 [24] Bailey H, Robertson BRD, Buckham BJ. Wave-to-wire simulation of a floating oscillating water
531 column wave energy converter. *Ocean Eng*
532 2016;125:248-60. <https://doi.org/10.1016/j.oceaneng.2016.08.017>
- 533 [25] Henriques JCC, Portillo JCC, Sheng W, Gato LMC, Falcão AFO. Dynamics and control of air
534 turbines in oscillating-water-column wave energy converters: Analyses and case study. *Renew*
535 *Sust Energ Rev* 2019;112:571-89. <https://doi.org/10.1016/j.rser.2019.05.010>
- 536 [26] Falcão AFO, Gato LMC, Nunes, E P A S. A novel radial self-rectifying air turbine for use in
537 wave energy converters. *Renew Energy* 2013;50:289-98.
538 <https://doi.org/10.1016/j.renene.2012.06.050>

- 539 [27] Fay F, Robles E, Marcos M, Aldaiturriaga E, Camacho EF. Sea trial results of a predictive
540 algorithm at the Mutriku Wave power plant and controllers assessment based on a detailed plant
541 model. *Renew Energy* 2020;146:1725-45. <https://doi.org/10.1016/j.renene.2019.07.129>
- 542 [28] Benreguig P, Kelly J, Pakrashi V, Murphy J. Wave-to-Wire Model Development and Validation
543 for Two OWC Type Wave Energy Converters. *Energies* 2019;12
544 <https://doi.org/10.3390/en12203977>
- 545 [29] Hirt CW, Nichols BD. Volume of fluid (VOF) method for the dynamics of free boundaries. *J*
546 *Comput Phys* 1981;39:201-25. [https://doi.org/10.1016/0021-9991\(81\)90145-5](https://doi.org/10.1016/0021-9991(81)90145-5)
- 547 [30] López I, Pereiras B, Castro F, Iglesias G. Holistic performance analysis and turbine-induced
548 damping for an OWC wave energy converter. *Renew Energy* 2016;85:1155-63.
549 <https://dx.doi.org/10.1016/j.renene.2015.07.075>
- 550 [31] Lisboa RC, Teixeira PRF, Torres FR, Didier E. Numerical evaluation of the power output of an
551 oscillating water column wave energy converter installed in the southern Brazilian coast. *Energy*
552 2018;162:1115-24. <https://doi.org/10.1016/j.energy.2018.08.079>
- 553 [32] López I, Carballo R, Iglesias G. Site-specific wave energy conversion performance of an
554 oscillating water column device. *Energy Conv Manag* 2019;195:457-65.
555 <https://doi.org/10.1016/j.enconman.2019.05.030>
- 556 [33] López I, Pereiras B, Castro F, Iglesias G. Performance of OWC wave energy converters:
557 influence of turbine damping and tidal variability. *Int J Energy Res* 2015;39:472-83.
558 <https://doi.org/10.1002/er.3239>
- 559 [34] López I, Castro A, Iglesias G. Hydrodynamic performance of an oscillating water column wave
560 energy converter by means of particle imaging velocimetry. *Energy* 2015;83:89-103.
561 <http://dx.doi.org/10.1016/j.energy.2015.01.119>
- 562 [35] López I, Pereiras B, Castro F, Iglesias G. Optimisation of turbine-induced damping for an OWC
563 wave energy converter using a RANS–VOF numerical model. *Appl Energy* 2014;127:105-14.
564 <https://doi.org/10.1016/j.apenergy.2014.04.020>
- 565 [36] Iglesias G, Carballo R. Wave energy potential along the Death Coast (Spain). *Energy*
566 2009;34:1963-75. <https://doi.org/10.1016/j.energy.2009.08.004>
- 567 [37] Carballo R, Arean N, Álvarez M, López I, Castro A, López M et al. Wave farm planning through
568 high-resolution resource and performance characterization. *Renew Energy* 2019;135:1097-107.
569 <https://doi.org/10.1016/j.renene.2018.12.081>
- 570 [38] Chakrabarti SK. Offshore structure modeling. Singapore: World Scientific, 1994
- 571 [39] López I, Carballo R, Taveira-Pinto F, Iglesias G. Sensitivity of OWC performance to air
572 compressibility. *Renew Energy* 2020;145:1334-47. <https://doi.org/10.1016/j.renene.2019.06.076>
- 573 [40] Simonetti I, Cappiotti L, Elsafti H, Oumeraci H. Evaluation of air compressibility effects on the
574 performance of fixed OWC wave energy converters using CFD modelling. *Renew Energy*
575 2018;119:741-53. <https://doi.org/10.1016/j.renene.2017.12.027>

- 576 [41] Falcão AFO, Henriques JCC. Model-prototype similarity of oscillating-water-column wave
577 energy converters. *Int J Mar Energy* 2014;6:18-34.
578 <https://dx.doi.org/10.1016/j.ijome.2014.05.002>
- 579 [42] Falcão AFO, Gato LMC. 8.05 - Air Turbines. In: Sayigh A, editor. *Comprehensive Renewable*
580 *Energy*, Oxford: Elsevier; 2012, p. 111-149. [https://dx.doi.org/10.1016/B978-0-08-087872-](https://dx.doi.org/10.1016/B978-0-08-087872-0.00805-2)
581 [0.00805-2](https://dx.doi.org/10.1016/B978-0-08-087872-0.00805-2)
- 582 [43] Elhanafi A, Macfarlane G, Fleming A, Leong Z. Experimental and numerical investigations on
583 the hydrodynamic performance of a floating–moored oscillating water column wave energy
584 converter. *Appl Energy* 2017;205:369-90. <https://doi.org/10.1016/j.apenergy.2017.07.138>
- 585 [44] Perez-Collazo C, Greaves D, Iglesias G. Hydrodynamic response of the WEC sub-system of a
586 novel hybrid wind-wave energy converter. *Energy Conv Manag*
587 2018;171:307-25. <https://doi.org/10.1016/j.enconman.2018.05.090>
- 588 [45] Hasselmann DE, Dunckel M, Ewing JA. Directional wave spectra observed during JONSWAP
589 1973. *J Phys Oceanogr* 1980;10:1264-80. [https://doi.org/10.1175/1520-0485\(1980\)010<](https://doi.org/10.1175/1520-0485(1980)010<1264:DWSODJ>2.0.CO;2)
590 [1264:DWSODJ>2.0.CO;2](https://doi.org/10.1175/1520-0485(1980)010<1264:DWSODJ>2.0.CO;2)
- 591